

Measuring tidal effects with the Einstein Telescope: A design studyAnna Puecher,^{1,2} Anuradha Samajdar^{3,*} and Tim Dietrich^{3,4}¹*Nikhef–National Institute for Subatomic Physics,**Science Park 105, 1098 XG Amsterdam, The Netherlands*²*Institute for Gravitational and Subatomic Physics (GRASP), Utrecht University,**Princetonplein 1, 3584 CC Utrecht, The Netherlands*³*Institut für Physik und Astronomie, Universität Potsdam, Haus 28, Karl-Liebknecht-Straße 24/25,
14476, Potsdam, Germany*⁴*Max Planck Institute for Gravitational Physics (Albert Einstein Institute),
Am Mühlenberg 1, Potsdam 14476, Germany*

(Received 12 April 2023; accepted 10 July 2023; published 20 July 2023)

Over the last few years, there has been a large momentum to ensure that the third-generation era of gravitational wave detectors will find its realisation in the next decades, and numerous design studies have been ongoing for some time. Some of the main factors determining the cost of the Einstein Telescope lie in the length of the interferometer arms and its shape; L-shaped detectors versus a single triangular configuration. Both designs are further expected to include a xylophone configuration for improvement on both ends of the frequency bandwidth of the detector. We consider binary neutron star sources in our study, as examples of sources already observed with the current-generation detectors and ones which hold most promise given the broader frequency band and higher sensitivity of the third-generation detectors. We estimate parameters of the sources, with different kinds of configurations of the Einstein Telescope detector, varying arm lengths, as well as shapes and alignments. Overall, we find little improvement with respect to changing the shape, or alignment. However, there are noticeable differences in the estimates of some parameters, including tidal deformability, when varying the arm length of the detectors. In addition, we also study the effect of changing the laser power, and the lower limit of the frequency band in which we perform the analysis.

DOI: [10.1103/PhysRevD.108.023018](https://doi.org/10.1103/PhysRevD.108.023018)**I. INTRODUCTION**

The observation of the first gravitational-wave (GW) signal from a binary neutron star (BNS) source, GW170817 [1] by the LIGO-Scientific [2], and Virgo [3] Collaborations, has provided a wealth of information, starting from constraining the expansion rate of the Universe [4,5], to establishing neutron-star mergers as one of the main cosmic sources of r -process elements [6–16], allowing a stringent bound on the speed of GWs [17], and placing constraints on alternative theories of gravity [18–21]. The supranuclear equation of state (EOS) was constrained from the observation of GW170817 [22,23]. Furthermore, the simultaneous observation of electromagnetic (EM) radiation observed with GW170817 [17,24,25] helped bounding the supranuclear EOS of neutron stars even more stringently [26–36].

As a detector with a much wider frequency band sensitive to GWs, the Einstein Telescope (ET) [37–41] promises to observe BNS signals for many cycles, increasing the detected signals' duration up to an hour. The analog

detector expected to be operational in the USA is Cosmic Explorer (CE) [42,43]. ET will certainly provide more constrained bounds on the neutron star EOS, even without an accompanying EM counterpart [44–50].

Unfortunately, it is very challenging to perform realistic studies exploiting the full capability of ET due to the wide frequency range it will cover and the large associated computational costs, however, numerous progress has been made regarding GW searches for ET signals, e.g., [51,52], and full parameter estimation (PE) studies, as discussed below. Reference [53] performed the first full Bayesian estimation study of GW signals from BNS sources observed by ET with a lower-frequency cutoff f_{low} of 5 Hz. For this, they constructed reduced order quadratures to make their study computationally feasible. Here, we perform PE using relative binning [54–56] to reduce the computational cost of our analysis. We use a lower frequency of $f_{\text{low}} = 6$ Hz, to provide realistic estimates of the source parameters, such as the chirp mass or the tidal deformability.

In the past, various PE studies have already been performed to estimate the Science returns to constrain tidal deformability from BNS observations in ET, including

*anuradha.samajdar@uni-potsdam.de

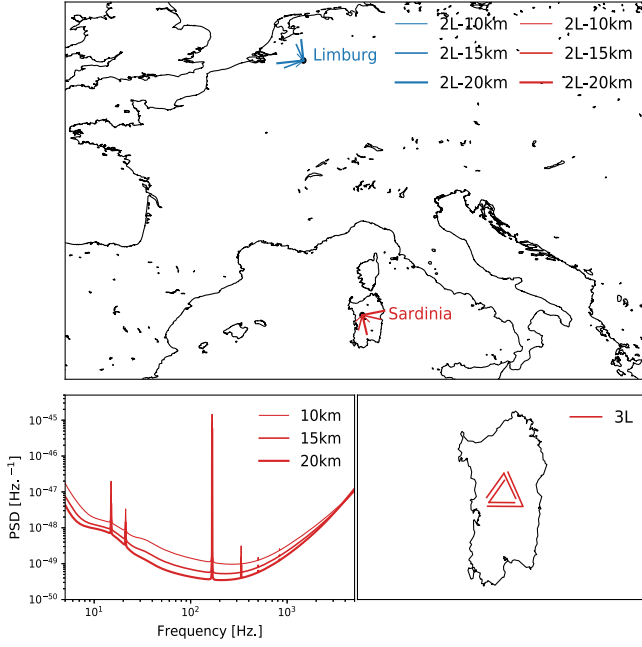


FIG. 1. Top panel: Location of the ET detectors in case of two L-shaped interferometers, showing also the possible different arm lengths in misaligned orientations. Bottom panel (left): Power spectral density (PSD) curves for the xylophone configuration in cryogenic mode for different arm lengths. Bottom panel (right): Representation of the ET triangular configuration, located in Sardinia for the purpose of this work.

using ET in a network of detectors e.g., [40,41,44–50] [53,57–71]. However, up to our knowledge, all of them have focused on the originally proposed triangular design with three interferometers, each having a 60° opening angle and arm length of 10 km, arranged in an equilateral triangle.

Recently, there has been an increasing interest in studying also different detector configurations and layouts. With this regard, Ref. [72] provided a detailed discussion with respect to numerous scientific cases and how they are affected by different proposed designs for ET, including different arm lengths and shapes. More explicitly, Ref. [72] considered the originally conceived triangular configuration, as well as two separate L-shaped detectors; for the latter, also different alignments, i.e., orientation between the detectors. In this study, we compare these different designs, cf. Fig. 1, for recovery of tidal deformability and the other parameters of BNS systems via full PE analysis. In all the studied cases, we analyze BNS simulations, and look at differing results from varying the detector setup, keeping the source properties of the BNS system and the settings of the PE analyses unchanged. Given the significant costs of ET, our study may provide useful information to make an estimate, based on the science returns, to reach a more informed decision about the final configuration of the detector. Some of our results have already been presented in [72], but in a much more compressed and less-detailed form.

We provide details of the PE methods in Sec. II and give the results of our study in Sec. III. We provide a summary and conclude in Sec. IV.

II. METHODS

Following standard techniques, we use a Bayesian analysis to construct posterior probability density functions (PDFs) on the parameters of interest, i.e., those characterizing the GW waveform describing a BNS merger. As we use quite low values of f_{low} to make our estimates realistic with what is envisaged for the ET detector, our likelihood integral calculation is computationally expensive. For this reason, we resort to the technique of relative binning following the analyses of GW170817 in [54–56]. This approach reduces our computational costs noticeably and makes our runs computationally feasible.

A. Bayesian analysis

In the employed Bayesian framework, all information about the parameters of interest is encoded in the PDF, given by Bayes’ theorem [73],

$$p(\vec{\theta}|\mathcal{H}_s, d) = \frac{p(d|\vec{\theta}, \mathcal{H}_s)p(\vec{\theta}|\mathcal{H}_s)}{p(d|\mathcal{H}_s)}, \quad (1)$$

where $\vec{\theta}$ is the set of parameter values and \mathcal{H}_s is the hypothesis that a GW signal depending on the parameters $\vec{\theta}$ is present in the data d . For parameter estimation purposes, the factor $p(d|\mathcal{H}_s)$, called the evidence for the hypothesis \mathcal{H}_s , is effectively set by the requirement that PDFs are normalized. Assuming the noise to be Gaussian, the likelihood $p(d|\vec{\theta}, \mathcal{H}_s)$ of obtaining data $d(f)$ given the presence of a signal $h(f)$ is determined by the proportionality

$$p(d|\vec{\theta}, \mathcal{H}_s) \propto \exp\left[-\frac{1}{2}(d - h|d - h)\right], \quad (2)$$

where the noise-weighted inner product $(\cdot|\cdot)$ is defined as

$$(d|h) = 4\Re \int_{f_{\text{low}}}^{f_{\text{high}}} \frac{\tilde{d}(f)\tilde{h}^*(f)}{S_h(f)} df. \quad (3)$$

Here a tilde refers to the Fourier transform, and $S_h(f)$ is the power spectral density (PSD).

Our choices for the prior probability density $p(\vec{\theta}|\mathcal{H}_s)$ in Eq. (1) are similar to what has been used for the analyses of real data when BNS signals were present with masses similar to GW170817. To sample the likelihood function in Eq. (2), we use the Bilby library [74,75], and specifically DYNesty [76,77] algorithm. The waveform we use for both signal injection and recovery is IMRPhenomD_NRTidalv2 [78–80].

B. Relative binning

The likelihood integral shown in Eq. (2) is constructed over a grid of frequencies and becomes computationally expensive as both the range of the integral grows, and as we analyze longer waveforms like those of BNS sources, which last for many cycles in the frequency band.

For our PE studies, we have varied f_{low} starting from 6 Hz up to 20 Hz, making the duration of the BNS signal in band from about 75 minutes to roughly 3 minutes, respectively. In addition, for an inference study to estimate parameters, we generate millions of waveforms, each associated with its own likelihood value for the sampling to get updated and for points to move towards higher likelihood regions. The method of relative binning [54–56] restricts the number of waveform evaluations by computing the likelihood from summary data calculated on a dense frequency grid for only one fiducial waveform, which must resemble the best fit to the data. The underlying assumption is that the set of parameters yielding a non-negligible contribution to the posterior probability produce similar waveforms, such that their ratio varies smoothly in the frequency domain. In this case, within each frequency bin $b = [f_{\text{min}}(b), f_{\text{max}}(b)]$, the ratio between the sampled waveforms and the fiducial one can be approximated by a linear function in frequency

$$r(f) = \frac{h(f)}{h_0(f)} = r_0(h, b) + r_1(h, b)(f - f_m(b)) + \dots, \quad (4)$$

where h_0 is the fiducial waveform and $f_m(b)$ the central frequency of the frequency bin b .

The coefficients $r_0(h, b)$ and $r_1(h, b)$ are computed for each sampled waveform, but can be determined from the values of $r(f)$ at the edges of the frequency bin b . Equation (3) can be written in terms of Eq. (4) and in a discrete form as

$$\langle d|h \rangle \approx \sum_b (A_0(b)r_0^*(h, b) + A_1(b)r_1^*(h, b)), \quad (5)$$

where the summary data

$$A_0(b) = 4 \sum_{f \in b} \frac{d(f)h_0^*(f)}{S_n(f)/T}, \quad (6)$$

$$A_1(b) = 4 \sum_{f \in b} \frac{d(f)h_0^*(f)}{S_n(f)/T} (f - f_m(b)), \quad (7)$$

are computed on the whole frequency grid, but only for the fiducial waveform.

For our purposes, we have followed the implementation outlined in [56] and the publicly available associated code [81]. We have, however, used the waveform `IMRPhenomD_NRTidalv2` [80] and employed the above code in

TABLE I. Source properties used for injections.

Name	m_1, m_2	\mathcal{M}_c	Λ_1, Λ_2	$\tilde{\Lambda}$	χ_1, χ_2
Source A	1.68, 1.13	1.19479	77, 973	303	0, 0
Source B	1.38, 1.37	1.19700	275, 309	292	0.02, 0.03
Source C	1.38, 1.37	1.19700	1018, 1063	1040	0, 0

conjunction with the sampling library `bilby`, employing the code in [82].

III. RESULTS

We consider three different sources (A, B, C) with parameters chosen following mainly the injection study performed by the LIGO-Virgo-KAGRA Collaboration [22] to mimic GW170817. The properties of the sources used for injections are listed in Table I, where m_i , χ_i , and Λ_i , with $i \in \{1, 2\}$ are, respectively, the mass, spin, and dimensionless tidal deformability of the component neutron star, while \mathcal{M}_c is the chirp mass and $\tilde{\Lambda}$ the binary's mass-weighted tidal deformability,

$$\tilde{\Lambda} = \frac{16(m_1 + 12m_2)m_1^4\Lambda_1 + (m_2 + 12m_1)m_2^4\Lambda_2}{3(m_1 + m_2)^5}. \quad (8)$$

All the simulated signals are injected at a distance $d_L = 100$ Mpc with inclination $\iota = 0.4$, zero polarization angle, and at a sky location $(\alpha, \delta) = (1.375, -1.211)$. The priors used for the analysis are reported in Table II, where $\delta\tilde{\Lambda}$ is defined as

$$\delta\tilde{\Lambda} = \frac{1}{2} \left[\sqrt{1-4\eta} \left(1 - \frac{13272}{1319}\eta + \frac{8944}{1319}\eta^2 \right) (\Lambda_1 + \Lambda_2) + \left(1 - \frac{15910}{1319}\eta + \frac{32850}{1319}\eta^2 + \frac{3380}{1319}\eta^3 \right) (\Lambda_1 - \Lambda_2) \right], \quad (9)$$

TABLE II. Priors employed in the PE analysis, where $\mathcal{M}_{c,s}$ represents the chirp-mass injected value of the specific source analyzed. For the luminosity distance d_L , the prior is taken uniform in comoving volume; for all the other parameters, the prior is uniform in the indicated range.

Parameter	Range
\mathcal{M}_c	$[\mathcal{M}_{c,s} \pm 0.05]$
q	$[0.5, 1]$
χ_1, χ_2	$[0.0, 0.15]$
d_L	$[1, 500]$
$\tilde{\Lambda}$	$[0, 5000]$
$\delta\tilde{\Lambda}$	$[-5000, 5000]$

TABLE III. Names used throughout this work for the different detector configurations and arm lengths.

Name	Shape	Relative orientation	Arm-length
Δ 10 km	Triangular		10 km
2L-0° 15 km	2 L-shaped	Aligned	15 km
2L-45° 15 km	2 L-shaped	Misaligned	15 km
2L-0° 20 km	2 L-shaped	Aligned	20 km
2L-45° 20 km	2 L-shaped	Misaligned	20 km
Δ 15 km	Triangular		15 km
2L-0° 10 km	2 L-shaped	Aligned	10 km
2L-45° 10 km	2 L-shaped	Misaligned	10 km

with $\eta = \frac{m_1 m_2}{(m_1 + m_2)^2}$ being the symmetric mass ratio of the binary.

Two different shapes have been proposed for ET in Ref. [72]: (i) a single detector with a triangular configuration, henceforth called Δ , and (ii) two L-shaped detectors in separate locations, with aligned or misaligned arms, henceforth called 2L-0° and 2L-45°, respectively. The Δ configuration consists of three V-shaped detectors, with each V having a 60° opening angle between the arms. For 2L-0°, the detectors have arms with the same orientation, while in the case of 2L-45° one detector has the arms rotated by 45° with the respect to the other one.

The Δ detector may have an armlength of 10 km or 15 km, while the L-shaped ones may have arm lengths of 15 km or 20 km. As of now, there are two main candidate sites for ET,¹ one in Sardinia (Italy), and one in Limburg (at the border shared by Netherlands, Belgium and Germany). In this paper, the Δ detector is located in Sardinia, whereas in the case of two L-shaped detectors one is in Sardinia and the other one in Limburg. All detector configurations used in our work are listed in Table III.

One of the main challenges to reach the sensitivity planned for ET is dealing with quantum noise, which includes shot noise at high frequencies and radiation pressure noise at low frequencies. A high laser power reduces shot noise, but a low laser power is instead required to reduce radiation pressure noise. To counter this problem, ET will be practically composed of two interferometers working together in a xylophone configuration, one detector optimized for low frequencies and with a low laser power, and the other one optimized at high frequencies and with a high power. Low-frequency sensitivity is also affected by thermal noise, therefore a further improvement is expected if the low-frequency detector operates at cryogenic temperatures [83].

¹Recently, also a third location in Saxony, Germany, has been considered as a possible site option.

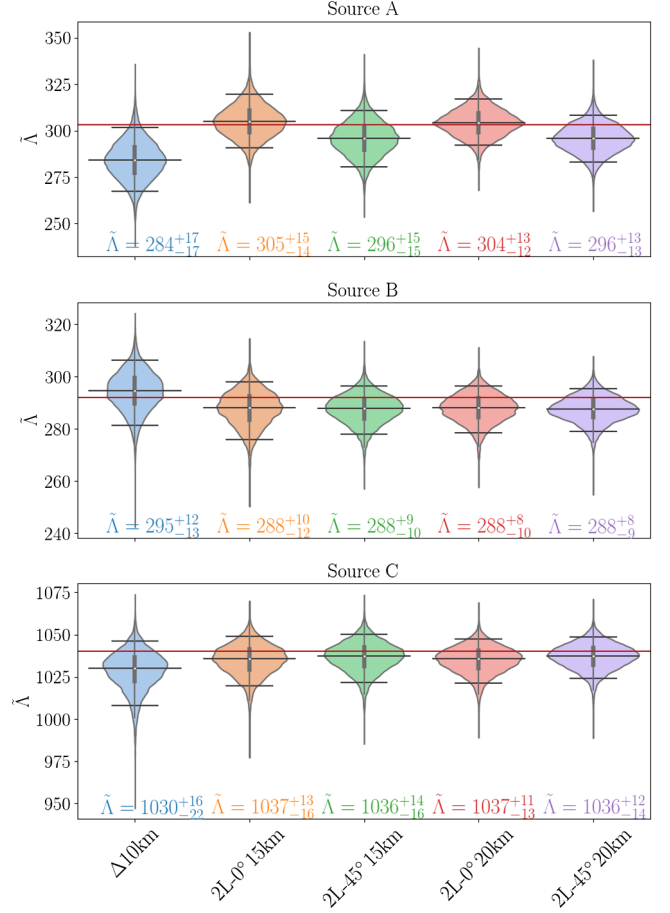


FIG. 2. Violin plots for the posterior density distribution of $\tilde{\Lambda}$ for the five reference detector configurations, and for all three sources in Table I: Source A (top panel), Source B (middle panel), and Source C (bottom panel). The black horizontal bars indicate the median value and the 90% confidence interval, the black vertical lines mark the support of the posterior; the red-horizontal line shows the injected value of $\tilde{\Lambda}$. For each posterior we also report the median, together with the 5% and 95% quantile values.

In this section we present the results of PE runs, comparing the different detector configurations, arm lengths and laser power. We also look at the improvement we get when analyzing data starting at different frequencies.

A. Detector configuration comparison

First, we test how the different detector configurations (Δ , 2L-0° or 2L-45°) perform in PE analyses. We take into account only the five reference configurations [72]; Δ with 10 km arms, 2L-0° and 2L-45°, both with 15 km or 20 km arms. For this comparison, all the runs are performed with starting frequency $f_{\text{low}} = 10$ Hz, and using the PSD curve for the xylophone configuration with the low frequency detector operating at cryogenic temperatures (LFHF). Figure 2 shows the posteriors for the tidal deformability parameter $\tilde{\Lambda}$ for the three different sources, reporting the median and 90% intervals for each configuration.

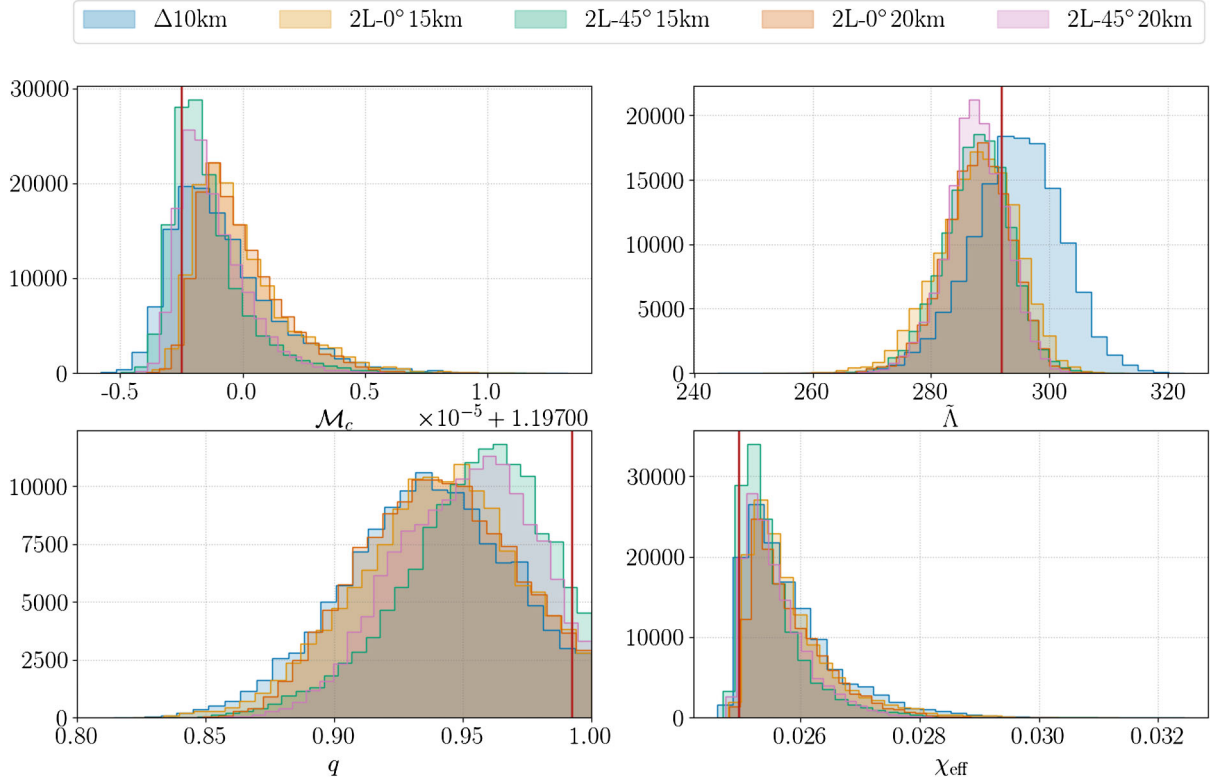


FIG. 3. Posteriors for chirp mass \mathcal{M}_c (top left), tidal deformability $\tilde{\Lambda}$ (top right), mass ratio q (bottom left), and effective spin χ_{eff} (bottom right), for Source B, cf. Table I. The different colors correspond to the various configurations considered, while the red line indicates the injected values.

For Source B, in Fig. 3 we show also the posterior distributions for the other binary parameters: chirp mass \mathcal{M}_c , mass ratio q and effective spin χ_{eff} , defined as

$$\chi_{\text{eff}} = \frac{\chi_1 m_1 + \chi_2 m_2}{m_1 + m_2}, \quad (10)$$

with χ_i and m_i being the spin and mass of the component neutron star. From Fig. 3 and especially from Fig. 2 we clearly see an improvement going from the Δ to the two L-shaped detectors, since, for example, the width of the 90% interval on $\tilde{\Lambda}$ reduces between 12% and 24% when going from the $\Delta 10$ km to the 2L-45° configuration. However, we must take into account the fact that the Δ detector here is assumed to have a shorter arm length, which has a great influence on the PSD, cf. Fig. 1. For this reason, we also compare the Δ and 2L configurations assuming they have the same arm length. Figure 4 shows Source C posteriors for \mathcal{M}_c , q , and $\tilde{\Lambda}$, for the different configurations, but assuming the same arm length. In this case, we do not see a strong difference in the parameters recovery, as indicated by the 5% and 95% quantile values reported in the plot. This suggests that the specific configuration does not have a major impact on the precision of parameter estimation. However, if the configuration choice is bound to a certain arm length, e.g., due to

limitations to the overall budget, one must take into account the improvements obtained with longer arms.

B. Effect of varying PSDs

As mentioned in the previous sections, the current plan for ET includes a “xylophone” configuration, in which each detector is effectively composed of two interferometers, operating a high- or low-power laser. The high-power laser is expected to improve sensitivity at high frequencies, the low-power one, on the other hand, improves sensitivity below 30 Hz [38,83]. We perform the same PE analysis using the PSD of the different interferometers and we compare results. In particular, we study the PSD for the detector optimized at high frequencies (HF-PSD), the one optimized at low frequencies (LF-PSD), and the xylophone combination (LFHF-PSD), with the low-frequency interferometer operating at cryogenic temperatures. Since we are interested in the PSD’s effect only, here we study just one source, Source C, and one detector configuration, $\Delta 10$ km, performing the analysis from a starting frequency $f_{\text{low}} = 10$ Hz. The posteriors for \mathcal{M}_c , q , $\tilde{\Lambda}$, and χ_{eff} are shown in Fig. 5, where we also report the median and the 5% and 95% quantiles for each parameter. The PSD optimized at low frequencies performs much worse than the other ones, with a 90% confidence interval 2.5 times

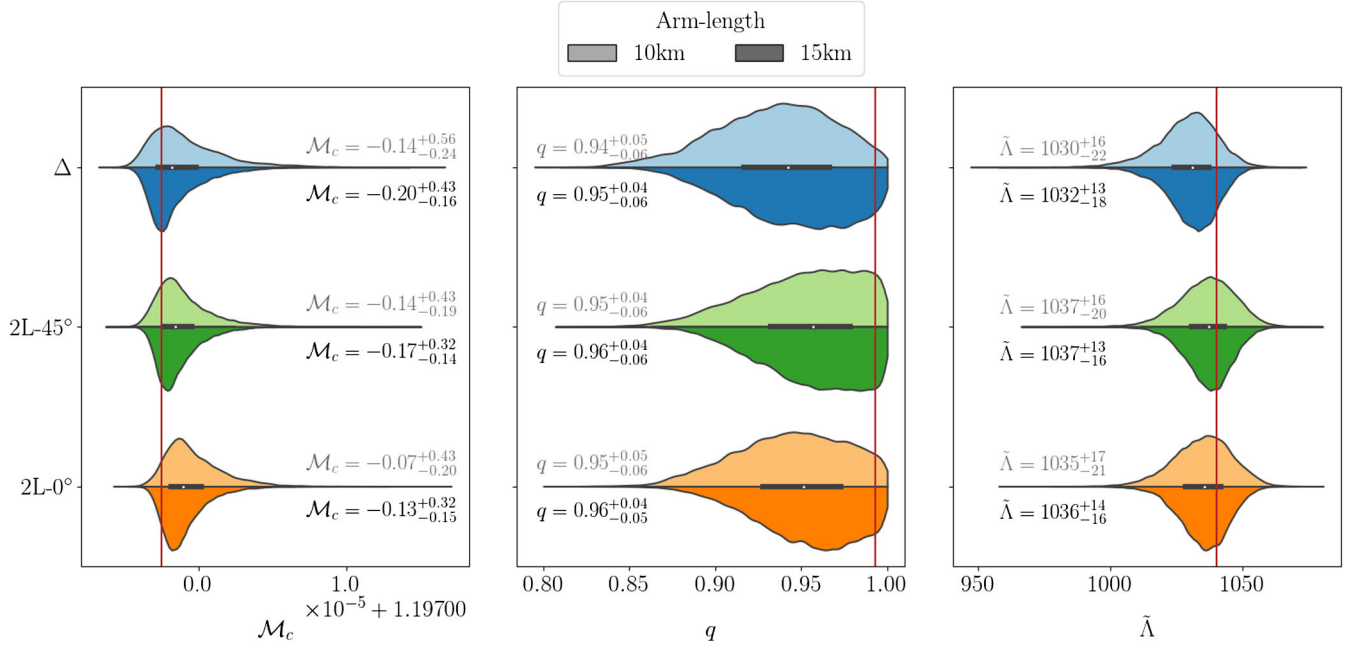


FIG. 4. Comparison of \mathcal{M}_c , $\tilde{\Lambda}$, and q posteriors between Δ , $2L-0^\circ$ and $2L-45^\circ$ with same arm-length, for Source C, cf. Table I. The darker color shade refers to detectors with 15 km arm length, the lighter one to detectors with 10 km arm-length. The red line indicates the parameter's injected value. For each parameter and configuration, we also report the median and 5% and 95% quantile values; for \mathcal{M}_c , also the reported values have an offset $\times 10^{-5} + 1.19700$.

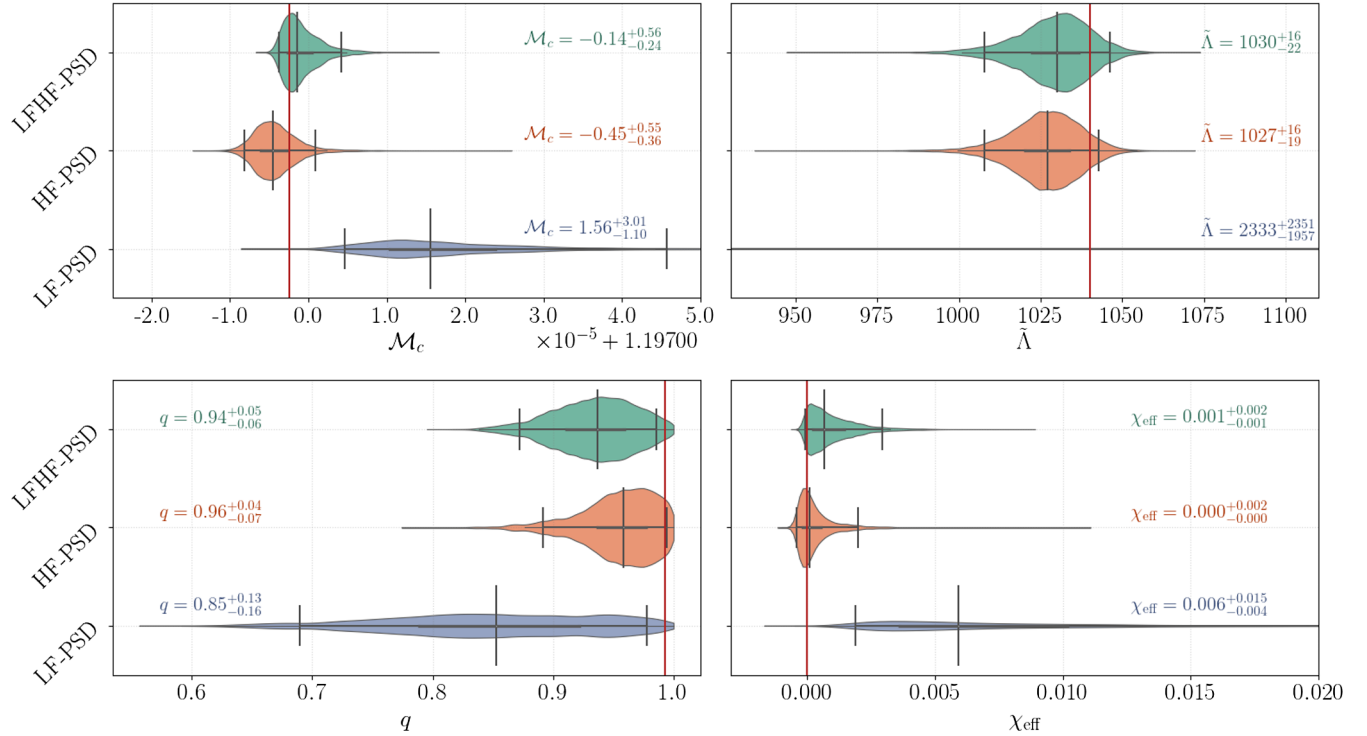


FIG. 5. Posteriors of \mathcal{M}_c , $\tilde{\Lambda}$, q , and χ_{eff} , for Source C (Table I) and the Δ 10 km configuration, recovered with the different PSDs. The vertical black lines show the median and the 90% confidence interval, while the black horizontal line indicates the support of the posterior; the red line shows the parameter's injected value. For \mathcal{M}_c , the reported median and quantile values have an offset $1 \times 10^{-5} + 1.19700$.

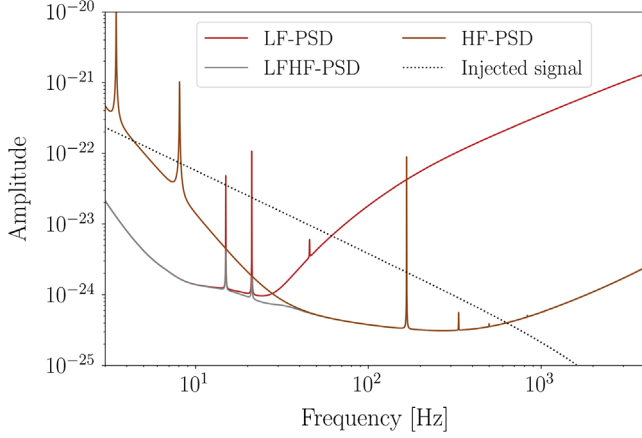


FIG. 6. Comparison between the PSD optimized at low frequencies (LF-PSD), in red, the PSD optimized at high frequencies (HF-PSD), in brown, and the one of the xylophone configuration (LFHF-PSD), in gray, with a typical injected GW signal (dotted line). All the PSDs shown refer to a detector with 10 km arm length. The sensitivity of the LF-PSD becomes too low at high frequencies to allow to detect the signal above ~ 100 Hz.

larger in the case of mass ratio. $\tilde{\Lambda}$ is not recovered with the LF-PSD, while it is constrained with an accuracy of almost 4% in the other cases. $\tilde{\Lambda}$ represents an extreme case, since its contribution enters the gravitational-wave phase mainly at high frequencies, from a few hundreds Hz and above [84,85], and therefore is affected by the shape of LF-PSD, as shown in Fig. 6, more than other parameters. In general, we obtain a much worse parameter recovery when using the LF-PSD alone, meaning that, if the preferred solution of a xylophone implementation is not available, the high-frequency optimized PSD is favorable, in particular if we want to constrain $\tilde{\Lambda}$.

C. Effect of varying minimum frequency

A big achievement of the ET is to improve the sensitivity at low frequencies. Therefore, in this section, we will study the impact of choosing different starting frequencies in the PE analysis. We note that lowering the starting frequency by only a few Hz has a huge impact on the duration of the waveform, and therefore of the computational cost of the analysis. We analyze injections with parameters of Source B, for two different configurations, $\Delta 10$ km, and $2L-45^\circ$ 15 km. In each case, we perform PE tests with the following starting frequencies: 6, 7, 8, 9, 10, and 20 Hz. In this case, the analysis is performed in zero noise, since we want to focus on the impact of f_{low} without risking to take into account possible fluctuations induced by the noise realizations. In fact, specific noise realizations can cause a shift in the posterior recovered for $\tilde{\Lambda}$. This shift is usually within 5% of the actual $\tilde{\Lambda}$ value, and, therefore, goes unnoticed in the analysis performed with current detectors. However, we

TABLE IV. Recovered $\tilde{\Lambda}$ values with 90% intervals, comparing Gaussian-noise and zero-noise runs for different values of f_{low} .

	f_{low}	Gaussian noise	Zero noise
$2L-45^\circ$ 15 km	7 Hz	$279.31^{+9.55}_{-11.35}$	$287.90^{+8.35}_{-9.54}$
	8 Hz	$292.90^{+8.40}_{-8.33}$	$287.36^{+9.01}_{-9.59}$
	9 Hz	$278.63^{+9.75}_{-10.72}$	$287.65^{+8.95}_{-10.92}$
	10 Hz	$285.74^{+11.15}_{-13.26}$	$287.40^{+9.03}_{-10.96}$
	20 Hz	$296.72^{+10.46}_{-11.66}$	$286.18^{+12.01}_{-14.42}$
$\Delta 10$ km	7 Hz	$277.27^{+11.87}_{-13.52}$	$287.29^{+10.95}_{-12.59}$
	8 Hz	$292.95^{+9.15}_{-9.77}$	$287.11^{+11.21}_{-12.79}$
	9 Hz	$274.62^{+12.78}_{-14.09}$	$285.51^{+11.71}_{-13.97}$
	10 Hz	$273.16^{+15.18}_{-17.09}$	$285.51^{+11.71}_{-13.97}$
	20 Hz	$280.09^{+13.76}_{-17.10}$	$285.21^{+14.56}_{-17.86}$

showed that for ET the precision with which $\tilde{\Lambda}$ can be measured improves noticeably. This means that, due to these shifts, we might end up seeing the injected values lying outside the posterior's 90% interval when simulations are done in Gaussian noise. When real ET data is being analyzed later, this is a point that must be evaluated very carefully. For our purposes, up to now, we compared only results obtained with the same f_{low} , and as long as we use the same noise seed, we expect a possible fluctuation to affect all the runs in the same way, and, therefore, to be not relevant in our comparison. Here, however, we use different starting frequency, leading to longer signals and more cycles being analyzed. In this case, the noise fluctuation's outcome can be different for the different f_{low} used. To quantify this, in Table IV we report the median and 90% interval values of the posteriors on $\tilde{\Lambda}$, obtained from analysis both in gaussian and zero noise, with the same seed but different f_{low} . While we see fluctuations in the median values recovered from Gaussian noise runs, in the zero noise case the median is almost constant. Therefore, to compare $\tilde{\Lambda}$ recovery with different starting frequency, we look at zero noise injections. Figure 7 shows the posteriors and their 90% width for the different f_{low} values. We see a clear improvement when going to lower frequencies, especially for the recovery of chirp mass. The plot also highlights how in general the $2L-45^\circ$ 15 km configuration yields tighter constraints on the parameters' posteriors, but we stress again that the main impact is given by the arm length, not the configuration *per se*.

IV. SUMMARY

We performed PE studies to compare the different proposed designs for ET. We focus on BNS systems, in particular, to find out how well the tidal effects will be measured. We compare different detector shapes, considering a single triangular detector and two L-shaped ones.

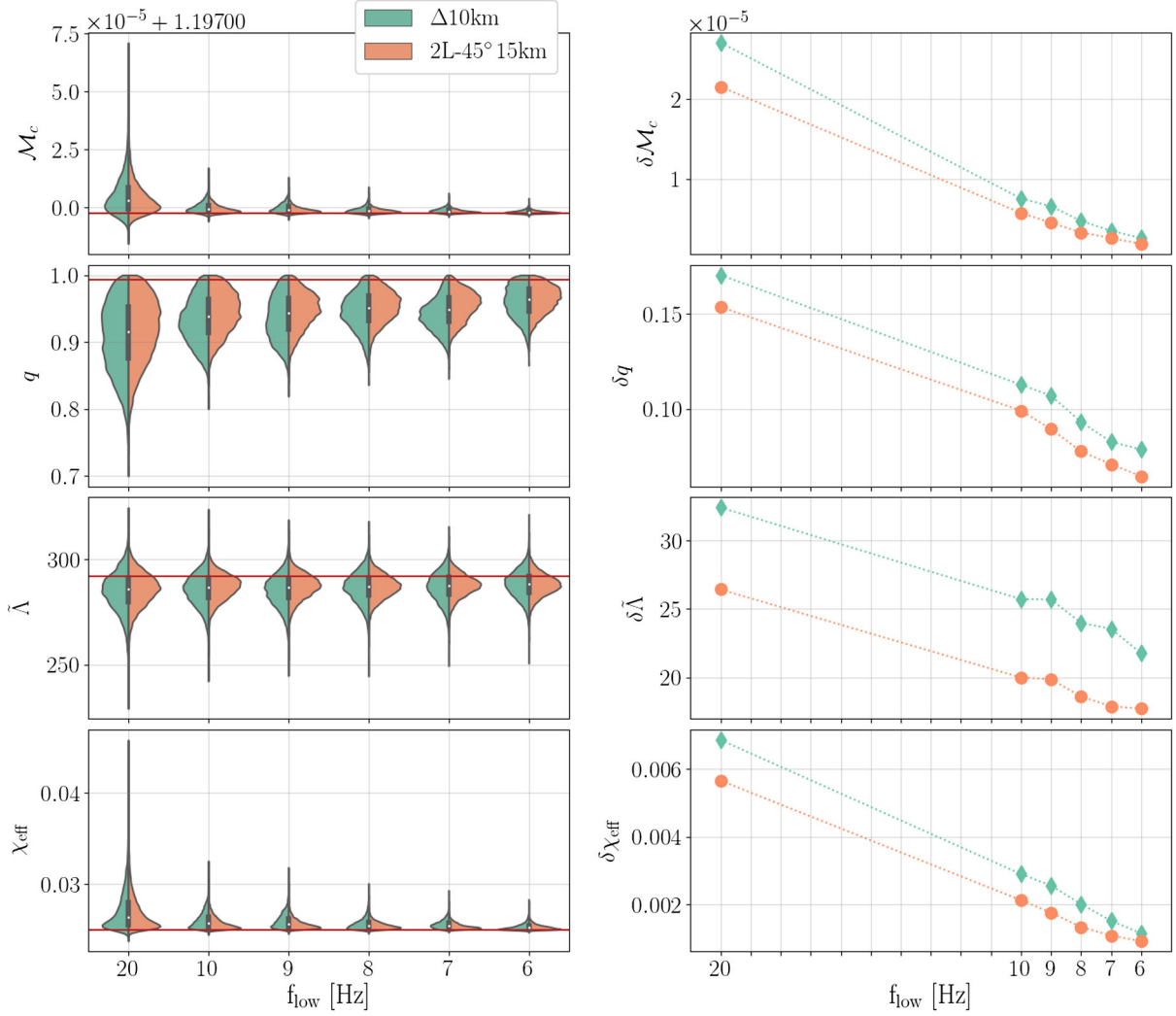


FIG. 7. Left: Posterior distributions for \mathcal{M}_c , q , $\tilde{\Lambda}$, and χ_{eff} for the different choices of f_{low} and for Source B (Table I), in green for the Δ configuration with 10 km arms, in orange for the 2L- 0° with 15 km arms. The red-horizontal lines correspond to the parameters' injected values. Right: Width of the 90% confidence interval for each parameter, as a function of the value of f_{low} .

In the latter case, we investigate both the cases of aligned or misaligned detectors. Moreover, ET will be composed of two interferometers, one optimized at high and one at low frequencies. We compared results obtained using the different PSDs, the low- and high-frequency one, as well as the xylophone PSD, obtained by combining the two. Finally, we looked at how the PE results improve when using lower cutoff frequencies, investigating $f_{\text{low}} = 20, 10, 9, 8, 7, 6$ Hz. We find that:

- (i) The shape and alignment of the detectors have very little influence on the recovery of parameters.²
- (ii) The chosen arm length, instead, plays an important role, as expected given its effect on the PSD. This means that, when comparing the currently proposed

²However, we want to point out that we have not include information from the null stream.

configurations, the Δ 10 km one performs worse, but this is merely due to the fact that it has a shorter arm length with respect to the 2L ones. When comparing the different configurations, and assuming the same arm length, we find no significant difference in the results.

- (iii) The constraints recovered with the LF-PSD are much worse than the other ones, especially with respect to $\tilde{\Lambda}$. This is expected since with the LF-PSD the signal above a hundred Hz is not detectable.
- (iv) Noise fluctuations have a very strong impact on the $\tilde{\Lambda}$ measurement, causing the posteriors' median values to shift. With ET, $\tilde{\Lambda}$ will be measured with a very high accuracy, therefore, although such shifts are of the order of a few percent, they can be enough for the injected value to lie outside the support of the posterior.

- (v) Regarding the different cutoff frequencies, we studied two different detector configurations, $\Delta 10$ km and $2L-45^\circ 15$ km, and find no substantial difference between them. The parameters posteriors become clearly tighter when going to lower frequencies. This is particularly evident in the case of \mathcal{M}_c posteriors, but an improvement is also present for $\tilde{\Lambda}$, but only of about 20%.

ACKNOWLEDGMENTS

A.P. is supported by the research programme of the Netherlands Organization for Scientific Research (NWO). This work was performed using the Computing Infrastructure of Nikhef, which is part of the research program of the Foundation for Nederlandse Wetenschappelijk Onderzoek Instituten (NWO-I), which is part of the Dutch Research Council

(NWO). A. S. thanks the Alexander von Humboldt foundation in Germany for a Humboldt fellowship for post-doctoral researchers. The authors are grateful for computational resources provided by the LIGO Laboratory and supported by the National Science Foundation Grants No. PHY-0757058 and No. PHY-0823459. Particularly, we thank Michael Thomas for prompt help with computing issues. This research has made use of data, software and/or web tools obtained from the Gravitational Wave Open Science Center ([86]), a service of LIGO Laboratory, the LIGO Scientific Collaboration, and the Virgo Collaboration. LIGO is funded by the U.S. National Science Foundation. Virgo is funded by the French Centre National de Recherche Scientifique (CNRS), the Italian Istituto Nazionale della Fisica Nucleare (INFN) and the Dutch Nikhef, with contributions by Polish and Hungarian institutes.

-
- [1] B. P. Abbott *et al.* (LIGO Scientific and Virgo Collaborations), *Phys. Rev. Lett.* **119**, 161101 (2017).
- [2] J. Aasi *et al.* (LIGO Scientific Collaboration), *Classical Quantum Gravity* **32**, 074001 (2015).
- [3] F. Acernese *et al.* (Virgo Collaboration), *Classical Quantum Gravity* **32**, 024001 (2015).
- [4] B. P. Abbott *et al.* (LIGO Scientific, VINROUGE, Las Cumbres Observatory, DLT40, Virgo, 1M2H, MASTER Collaborations), *Nature (London)* **551**, 85 (2017).
- [5] M. Bulla, M. W. Coughlin, S. Dhawan, and T. Dietrich, *Universe* **8**, 289 (2022).
- [6] D. Eichler, M. Livio, T. Piran, and D. N. Schramm, *Nature (London)* **340**, 126 (1989).
- [7] S. Rosswog, M. Liebendoerfer, F. K. Thielemann, M. B. Davies, W. Benz, and T. Piran, *Astron. Astrophys.* **341**, 499 (1999).
- [8] P. S. Cowperthwaite *et al.*, *Astrophys. J.* **848**, L17 (2017).
- [9] S. J. Smartt *et al.*, *Nature (London)* **551**, 75 (2017).
- [10] M. M. Kasliwal *et al.*, *Science* **358**, 1559 (2017).
- [11] D. Kasen, B. Metzger, J. Barnes, E. Quataert, and E. Ramirez-Ruiz, *Nature (London)* **551**, 80 (2017).
- [12] N. R. Tanvir *et al.*, *Astrophys. J.* **848**, L27 (2017).
- [13] S. Rosswog, J. Sollerman, U. Feindt, A. Goobar, O. Korobkin, R. Wollaeger, C. Fremling, and M. M. Kasliwal, *Astron. Astrophys.* **615**, A132 (2018).
- [14] B. P. Abbott *et al.* (LIGO Scientific and Virgo Collaborations), *Astrophys. J.* **850**, L39 (2017).
- [15] S. Ascenzi *et al.*, *Mon. Not. R. Astron. Soc.* **486**, 672 (2019).
- [16] D. Watson *et al.*, *Nature (London)* **574**, 497 (2019).
- [17] B. P. Abbott *et al.* (LIGO Scientific, Virgo, Fermi GBM, INTEGRAL, IceCube, AstroSat Cadmium Zinc Telluride Imager Team, IPN, Insight-Hxmt, ANTARES, Swift, AGILE Team, 1M2H Team, Dark Energy Camera GW-EM, DES, DLT40, GRAWITA, Fermi-LAT, ATCA, ASKAP, Las Cumbres Observatory Group, OzGrav, DWF (Deeper Wider Faster Program), AST3, CAASTRO, VINROUGE, MASTER, J-GEM, GROWTH, JAGWAR, CaltechNRAO, TTU-NRAO, NuSTAR, Pan-STARRS, MAXI Team, TZAC Consortium, KU, Nordic Optical Telescope, ePESSTO, GROND, Texas Tech University, SALT Group, TOROS, BOOTES, MWA, CALET, IKI-GW Follow-up, H.E.S.S., LOFAR, LWA, HAWC, Pierre Auger, ALMA, Euro VLBI Team, Pi of Sky, Chandra Team at McGill University, DFN, ATLAS Telescopes, High Time Resolution Universe Survey, RIMAS, RATIR, SKA South Africa/MeerKAT), *Astrophys. J. Lett.* **848**, L12 (2017).
- [18] J. M. Ezquiaga and M. Zumalacárregui, *Phys. Rev. Lett.* **119**, 251304 (2017).
- [19] T. Baker, E. Bellini, P. G. Ferreira, M. Lagos, J. Noller, and I. Sawicki, *Phys. Rev. Lett.* **119**, 251301 (2017).
- [20] P. Creminelli and F. Vernizzi, *Phys. Rev. Lett.* **119**, 251302 (2017).
- [21] J. Sakstein and B. Jain, *Phys. Rev. Lett.* **119**, 251303 (2017).
- [22] B. P. Abbott *et al.* (LIGO Scientific and Virgo Collaborations), *Phys. Rev. X* **9**, 011001 (2019).
- [23] B. P. Abbott *et al.* (LIGO Scientific and Virgo Collaborations), *Phys. Rev. Lett.* **121**, 161101 (2018).
- [24] B. P. Abbott *et al.* (LIGO Scientific, Virgo, Fermi-GBM, and INTEGRAL Collaborations), *Astrophys. J. Lett.* **848**, L13 (2017).
- [25] B. P. Abbott *et al.* (LIGO Scientific and Virgo Collaborations), *Astrophys. J. Lett.* **850**, L39 (2017).
- [26] A. Bauswein, O. Just, H.-T. Janka, and N. Stergioulas, *Astrophys. J.* **850**, L34 (2017).
- [27] M. Ruiz, S. L. Shapiro, and A. Tsokaros, *Phys. Rev. D* **97**, 021501 (2018).
- [28] D. Radice, A. Perego, F. Zappa, and S. Bernuzzi, *Astrophys. J.* **852**, L29 (2018).

- [29] E. R. Most, L. R. Weih, L. Rezzolla, and J. Schaffner-Bielich, *Phys. Rev. Lett.* **120**, 261103 (2018).
- [30] M. W. Coughlin, T. Dietrich, B. Margalit, and B. D. Metzger, *Mon. Not. R. Astron. Soc.* **489**, L91 (2019).
- [31] C. D. Capano, I. Tews, S. M. Brown, B. Margalit, S. De, S. Kumar, D. A. Brown, B. Krishnan, and S. Reddy, *Nat. Astron.* **4**, 625 (2020).
- [32] T. Dietrich, M. W. Coughlin, P. T. H. Pang, M. Bulla, J. Heinzl, L. Issa, I. Tews, and S. Antier, *Science* **370**, 1450 (2020).
- [33] M. Breschi, A. Perego, S. Bernuzzi, W. Del Pozzo, V. Nedora, D. Radice, and D. Vescovi, *Mon. Not. R. Astron. Soc.* **505**, 1661 (2021).
- [34] M. Nicholl, B. Margalit, P. Schmidt, G. P. Smith, E. J. Ridley, and J. Nuttall, *Mon. Not. R. Astron. Soc.* **505**, 3016 (2021).
- [35] G. Raaijmakers *et al.*, *Astrophys. J.* **922**, 269 (2021).
- [36] S. Huth *et al.*, *Nature (London)* **606**, 276 (2022).
- [37] A. Freise, S. Chelkowski, S. Hild, W. Del Pozzo, A. Perreca, and A. Vecchio, *Classical Quantum Gravity* **26**, 085012 (2009).
- [38] S. Hild, S. Chelkowski, A. Freise, J. Franc, N. Morgado, R. Flaminio, and R. DeSalvo, *Classical Quantum Gravity* **27**, 015003 (2010).
- [39] M. Punturo *et al.*, *Classical Quantum Gravity* **27**, 194002 (2010).
- [40] B. Sathyaprakash *et al.*, in *46th Rencontres de Moriond on Gravitational Waves and Experimental Gravity* (The Gioi Publishers, Vietnam, 2011), pp. 127–136, arXiv:1108.1423.
- [41] M. Maggiore *et al.*, *J. Cosmol. Astropart. Phys.* **03** (2020) 050.
- [42] M. Evans *et al.*, arXiv:2109.09882.
- [43] D. Reitze *et al.*, *Bull. Am. Astron. Soc.* **51**, 035 (2019).
- [44] C. Pacilio, A. Maselli, M. Fasano, and P. Pani, *Phys. Rev. Lett.* **128**, 101101 (2022).
- [45] A. Maselli, A. Sabatucci, and O. Benhar, *Phys. Rev. C* **103**, 065804 (2021).
- [46] A. Sabatucci, O. Benhar, A. Maselli, and C. Pacilio, *Phys. Rev. D* **106**, 083010 (2022).
- [47] F. Iacovelli, M. Mancarella, S. Foffa, and M. Maggiore, *Astrophys. J.* **941**, 208 (2022).
- [48] N. Williams, G. Pratten, and P. Schmidt, *Phys. Rev. D* **105**, 123032 (2022).
- [49] M. Breschi, S. Bernuzzi, D. Godzieba, A. Perego, and D. Radice, *Phys. Rev. Lett.* **128**, 161102 (2022).
- [50] H. Rose, N. Kunert, T. Dietrich, P. T. H. Pang, R. Smith, C. Van Den Broeck, S. Gandolfi, and I. Tews, arXiv:2303.11201.
- [51] D. Meacher, K. Cannon, C. Hanna, T. Regimbau, and B. Sathyaprakash, *Phys. Rev. D* **93**, 024018 (2016).
- [52] S. Wu and A. H. Nitz, *Phys. Rev. D* **107**, 063022 (2023).
- [53] R. Smith *et al.*, *Phys. Rev. Lett.* **127**, 081102 (2021).
- [54] B. Zackay, L. Dai, and T. Venumadhav, arXiv:1806.08792.
- [55] L. Dai, T. Venumadhav, and B. Zackay, arXiv:1806.08793.
- [56] N. Leslie, L. Dai, and G. Pratten, *Phys. Rev. D* **104**, 123030 (2021).
- [57] B. S. Sathyaprakash, B. F. Schutz, and C. Van Den Broeck, *Classical Quantum Gravity* **27**, 215006 (2010).
- [58] C. Van Den Broeck, in *12th Marcel Grossmann Meeting on General Relativity* (World Scientific, Singapore, 2011), pp. 1682–1685, arXiv:1003.1386.
- [59] W. Zhao, C. Van Den Broeck, D. Baskaran, and T. G. F. Li, *Phys. Rev. D* **83**, 023005 (2011).
- [60] M. Punturo *et al.*, *Classical Quantum Gravity* **27**, 084007 (2010).
- [61] B. Sathyaprakash *et al.*, *Classical Quantum Gravity* **29**, 124013 (2012); **30**, 079501(E) (2013).
- [62] C. Van Den Broeck, *J. Phys. Conf. Ser.* **484**, 012008 (2014).
- [63] B. S. Sathyaprakash *et al.*, arXiv:1903.09221.
- [64] A. Samajdar and T. Dietrich, *Phys. Rev. D* **101**, 124014 (2020).
- [65] A. H. Nitz and T. Dal Canton, *Astrophys. J. Lett.* **917**, L27 (2021).
- [66] M. L. Chan, C. Messenger, I. S. Heng, and M. Hendry, *Phys. Rev. D* **97**, 123014 (2018).
- [67] W. Zhao and L. Wen, *Phys. Rev. D* **97**, 064031 (2018).
- [68] F. Hernandez Vivanco, R. Smith, E. Thrane, P. D. Lasky, C. Talbot, and V. Raymond, *Phys. Rev. D* **100**, 103009 (2019).
- [69] G. Castro, L. Gualtieri, A. Maselli, and P. Pani, *Phys. Rev. D* **106**, 024011 (2022).
- [70] A. Puecher, T. Dietrich, K. W. Tsang, C. Kalaghatgi, S. Roy, Y. Setyawati, and C. Van Den Broeck, *Phys. Rev. D* **107**, 124009 (2023).
- [71] S.-J. Jin, T.-N. Li, J.-F. Zhang, X. Zhang, arXiv:2202.11882.
- [72] M. Branchesi *et al.*, arXiv:2303.15923.
- [73] J. Veitch and A. Vecchio, *Phys. Rev. D* **81**, 062003 (2010).
- [74] G. Ashton *et al.*, *Astrophys. J. Suppl. Ser.* **241**, 27 (2019).
- [75] I. M. Romero-Shaw *et al.*, *Mon. Not. R. Astron. Soc.* **499**, 3295 (2020).
- [76] J. S. Speagle, *Mon. Not. R. Astron. Soc.* **493**, 3132 (2020).
- [77] S. Kuposov *et al.*, joshspeagle/dynesty: v1.2.2 (2022), 10.5281/zenodo.6456387.
- [78] T. Dietrich, S. Bernuzzi, and W. Tichy, *Phys. Rev. D* **96**, 121501 (2017).
- [79] T. Dietrich *et al.*, *Phys. Rev. D* **99**, 024029 (2019).
- [80] T. Dietrich, A. Samajdar, S. Khan, N. K. Johnson-McDaniel, R. Dudi, and W. Tichy, *Phys. Rev. D* **100**, 044003 (2019).
- [81] N. Leslie, L. Dai, and G. Pratten, Modebymode-relative-binning (2021), <https://github.com/nathaniel-leslie/modebymode-relative-binning>.
- [82] J. Janquart, RELATIVEBILBYING: A package for relative binning with Bilby, <https://github.com/lemnis12/relativebilbying> (2022).
- [83] S. Hild *et al.*, *Classical Quantum Gravity* **28**, 094013 (2011).
- [84] T. Dietrich, T. Hinderer, and A. Samajdar, *Gen. Relativ. Gravit.* **53**, 27 (2021).
- [85] I. Harry and T. Hinderer, *Classical Quantum Gravity* **35**, 145010 (2018).
- [86] <https://www.gw-openscience.org>.